RSC Advances

PAPER

View Article Online
View Journal | View Issue

Cite this: *RSC Adv.*, 2025, **15**, 29367

A facile *in situ* integration of red mud-derived metal oxides into graphene sheets for sulfamethoxazole removal from water

Nguyen Thi Mai,[ab] Le Thi Thanh Hoa,[c] Dang Van Thanh,[*bc] Nguyen Nhat Huy,[de] Hoang Minh Trang,[bf] Tran Van Son,[b] Pham Thi Thuy,[b] Nguyen Thi An Hang,[g] Tran Thi Minh Hang[bf] and Nguyen Manh Khai[*bf]

In this study, we present a facile *in situ* integration of red mud-derived metal oxides into graphene sheets *via* an electrochemical method, and we demonstrate its application for sonodegradation of sulfamethoxazole (SMX) in water. The resulting red mud-derived metal oxides/graphene composite (RAG) has a porous structure (with a specific surface area of 42.08 $m^2\ g^{-1}$) and contains metal oxides (*e.g.*, TiO_2, Al_2O_3, and Fe_2O_3) and SiO_2 anchored on the surface of the exfoliated graphite flakes *via* oxygen bridges (*e.g.*, C–O–Ti/Al/Fe). The produced nanocomposites contained Fe^{2+} and Fe^{3+} with a vital role in sonochemical degradation and the oxygen-containing groups such as COOH, C–O–C, and C=O for attracting the pollutant molecules to the catalyst surface. The investigated results of SMX degradation indicated an excellent performance of the synthesized RAGs with the highest SMX degradation efficiency of 91.5% at pH 7, SMX initial concentration of 10 mg L^{-1}, catalyst dosage of 0.5 g L^{-1}, volume of 100 mL, temperature of 313 K, and reaction time of 180 min. Besides, the SMX degradation can occur at a wide pH range of 3–7, suggesting a potential solution for removing antibiotic pollutants in environmental remediation.

Received 20th June 2025
Accepted 14th August 2025

DOI: 10.1039/d5ra04400f

rsc.li/rsc-advances

1. Introduction

Red mud (RM) usually consists of Fe_2O_3 (54%), Al_2O_3 (16.4%), SiO_2 (5.14%), TiO_2 (6.88%), Na_2O (3.32%), and several others (Zn, Ba, Hg, Sn, Be…), which is a waste of the process producing alumina by bauxite ore following Bayer technology. It contains smooth particles with a clay ratio of 17.2% and limon ratio of 47.5%, high total iron content (about 21.6%),[1,2] and it is one of the most important waste problems of the alumina industry. The most harmful factor of red mud is its high pH (pH > 12) which destroys or harms creatures contact directly with the waste and degrades the quality of surface and underground water.[3–5] Therefore, finding a way to reuse red mud as useful material is a research direction which attracted the attention of the scientists in recent years.

Sulfamethoxazole (SMX), introduced in the United States in 1961, is one of the most popular oral sulfonamide antibiotics which is usually used to treat and prevent a variety of uncomplicated bacterial infections of the urinary tract, respiratory system, and gastrointestinal tract.[6] The used amount for SMX is about 8 million prescriptions each year.[7] The half-life of SMX in the kidney is about 7–10 hours,[8] thus it is difficult to decompose in the aqueous environment. To eliminate SMX in water, several methods have been used such as Sponge-MBR combined with ozonation, sonodegradation, adsorption, or using nanomaterials (*e.g.*, nano-TiO_2, MgO@CNT, and rGO/CdW_4) to enhance the degradation capacity of SMX. Besides, ozonation combined with chlorination, anodic oxidation using metal oxide anodes,[9] electro-Co^{2+}/peroxydisulfate system with the cathode of activated carbon fiber,[10] UV light, UV/H_2O_2, and UV/$S_2O_8^{2-}$,[11,12] boron-doped diamond electrode,[12] and combination of graphite/graphene with other metal oxides also showed great and effective potential for removal antibiotics in an aqueous environment. However, these works consumed lots of chemicals to modify raw materials or required chemical precursors with high-quality accompanying time-consuming preparation materials. Additionally, the direct utilization of metal oxides

[a]*Thai Nguyen University of Agriculture and Forestry, Quyet Thang, Thai Nguyen, Vietnam*

[b]*Faculty of Environmental Sciences, University of Science, Vietnam National University, Hanoi, 334 Nguyen Trai, Thanh Xuan, Hanoi, Vietnam*

[c]*Thai Nguyen University of Medicine and Pharmacy, 284 Luong Ngoc Quyen, Thai Nguyen, Vietnam. E-mail: thanhdv@tnmc.edu.vn*

[d]*Faculty of Environment and Natural Resources, Ho Chi Minh City University of Technology (HCMUT), 268 Ly Thuong Kiet Street, Ho Chi Minh City, Vietnam*

[e]*Vietnam National University, Ho Chi Minh City, Linh Trung Ward, Thu Duc City, Ho Chi Minh City, Vietnam*

[f]*VNU Key Laboratory of Green Environment Technology and Waste Utilization (GreenLab), University of Science, Vietnam National University, 334 Nguyen Trai Road, Thanh Xuan, Hanoi 100000, Vietnam*

[g]*Faculty of Advanced Technologies and Engineering, VNU Vietnam Japan University, Luu Huu Phuoc St., Tu Liem., Hanoi 12015, Vietnam*

and high pH of red mud as raw material to fabricate the material with high ability for removing antibiotics in aqueous solutions has not been reported.

In the present work, we proposed a simple and effective method for the anchoring of metal oxides on the graphene sheets by direct activation of graphite in basic red mud slurry. This eco-friendly process addresses the issues of (i) reuse of waste red mud slurry, (ii) utilization of the high alkaline condition of RM slurry as both electrolyte and catalyst for simultaneous activating and exfoliating of graphite, and (iii) *in situ* integration of metal oxides nanostructures into graphene layers. Various characterizations were then applied to fully understand the formation of the composite material and the interaction of red mud components and graphene in the composite. The applicability of the produced material was evaluated through a sulfamethoxazole (SMX) removal test in water using RAG composite as the agent of the sonodegradation process. This study provides a potential solution to prevent environmental impacts while developing technologies to recover and reuse red mud for other purposes. It is believed that the viewpoint of industrial waste as a resource would contribute significantly to environmental protection.

2. Experimental

2.1. Synthesis and characterization of materials

Fig. 1 is the schematic presentation of red mud-activated graphite formation for eliminating SMX. In a typical procedure, 450 mL of red mud slurry (taken from Tan Rai aluminum factory, Lam Dong Province, Vietnam) was added with 100 mL of 5% w/w $(NH_4)_2SO_4$ solution. Graphite rod (99.99%) was then electrochemically activated and exfoliated simultaneously using this electrolyte under a working voltage of 39.9 V and a current intensity of 2.75 A for 2, 3, 4, 5, or 6 h. Under the electric current, the graphite rod was exfoliated and dispersed into the solution. The suspension was then cooled to ambient temperature and the resulting material was collected by filtration, washed with distilled water, and dried at 100 °C for 24 h. The obtained red mud-activated graphene composite powder (denoted as RAG) was finally placed in a desiccator at 30 °C. The samples were named RAG 2, RAG 3, RAG 4, RAG 5, and RAG 6, respectively. For comparison purposes, electrochemically exfoliated graphite (EEG) was also prepared by using the mixture of $(NH_4)_2SO_4$ (5%, 50 mL) and KOH (7.5%, 300 mL) instead of red mud slurry.

The produced materials were then characterized by Raman spectroscopy (HORIBA, Lab RAM HR 800), high-resolution transmission electron microscopy (HRTEM, JEOL 2100F), field emission scanning electron microscopy (FESEM, Hitachi SU8000), X-ray photoelectron spectroscopy (XPS, Thermo Scientific™ ESCALAB™ XI+ X-ray Photoelectron Spectrometer), Brunauer–Emmett–Teller analysis (BET, TriStar 3000), Fourier-transform infrared spectroscopy (FTIR, Shimadzu IR Prestige-21), and X-ray diffraction (XRD, D2 Phaser) to explore their properties.

2.2. Sonodegradation of SMX

The sonodegradation of SMX was investigated with several factors such as pH (3–11), initial concentration of SMX (10 mg L^{-1}), contact time (30, 60, 90, 120, 150, and 180 min), catalyst dose (0.1–0.6 g L^{-1}), and temperature (30, 40, and 50 °C). NaOH and HCl solutions were used to adjust the pH value of the solution. Typically, 0.03 g of RAG was added into an Erlenmeyer flask containing 100 mL of SMX solution. After that, the resulting mixture was deposited into an ultrasound bath with an ultrasound frequency of 40 kHz and power of 600 W. The mixture was sonicated continuously at these stable conditions

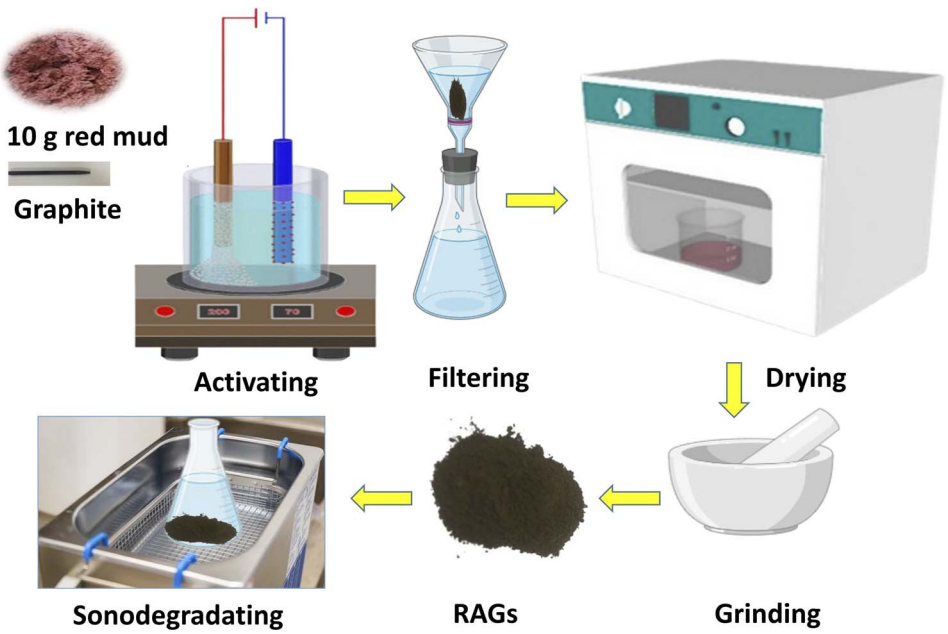

Fig. 1 The schematic presentation of red mud-activated graphite composite formation for sonodegradation of SMX in water.

for 3 h. After each 30 min, 5 mL of the mixture was taken and centrifuged at a speed of 6000 rpm min^{-1} for 10 min to remove the solids. The supernatant was taken to measure the absorbance at a wavelength of 274 nm using a UV-Vis spectrophotometer (Hitachi UH5300 UV-Vis). The SMX removal efficiency (E, %) and pseudo-first-order rate constant (k, min^{-1}) are calculated by the following equations.

$$E = \frac{C_0 - C_t}{C_0} \times 100\% \quad (1)$$

$$\ln\frac{C_0}{C_t} = k \times t \quad (2)$$

where C_0 and C_t (mg L^{-1}) are the initial concentration and concentration at t (min) of SMX.

Additionally, the activation energy (E_a) and thermodynamic parameters ($\Delta G°$, $\Delta H°$, $\Delta S°$) of the reaction are also vital values. They indicate the feasibility of the degradation process as well as the tendency of reaction. The activation energy can be obtained from the Arrhenius equation (eqn (3)), whereas the thermodynamic parameters are calculated *via* eqn (4)–(6).

$$\ln k = \frac{-E_a}{R}\left(\frac{1}{T}\right) + \ln A \quad (3)$$

$$\Delta H^\circ = E_a - RT \quad (4)$$

$$\Delta S^\circ = R\left(\ln A - \ln\frac{k_B T}{h} - 1\right) \quad (5)$$

$$\Delta G^\circ = \Delta H^\circ - T \times \Delta S^\circ \quad (6)$$

where A is a constant, R is the ideal gas constant (R = 8.314 J mol^{-1} K^{-1}), T (K) is the temperature, k_B is Boltzmann constant ($k_B = 1.381 \times 10^{-23}$ J K^{-1}), and h is Planck constant ($h = 6.626176 \times 10^{-34}$ J s^{-1}).

3. Results and discussion

3.1. Characterizations of RAGs

Fig. 2a–c displays the SEM images of red mud, EEG, and RAG composite, respectively. It can be seen that red mud contains nanoparticles arranged to form a porous structure, whereas EEG consists of stacked, thin sheets. The obtained RAGs indicated the presence of thin sheets of graphene and nanoparticles of red mud, which can be further confirmed by TEM images inset Fig. 2c. More graphene sheets were observed when the exfoliation time increased from 3 h to 6 h demonstrating the content of EEG or intensity of graphene's peaks, which was further confirmed by FT-IR and XRD data are shown in Fig. 2d and e. It can be observed from the inset of Fig. 2d that the small and narrow peaks at 2θ = 9.73° and 43.71° correspond to the (002) and (101) crystalline planes of graphene flakes[13] while a sharp and high peak at 2θ = 26.25° can be assigned to (100) crystalline plane of graphite.[14] Meanwhile, the XRD spectra of red mud indicated the small peak at 2θ = 14.03°, attributed to the mineral component of $Na_5Al_3CSi_3O_{15}$, which then disappeared when combined with graphene flakes due to the change to amorphous phase or other components. Simultaneously, the peak of $Na_5Al_3CSi_3O_{15}$ was also exhibited at 2θ = 24.34°, whose intensity decreased when RM was combined with exfoliated graphite flakes. However, the intensity increased with the increase of the electrochemical time from 2 h to 5 h, followed by a slight decrease with the electrochemical time of 6 h. Besides, it was also found the peaks of muscovite mineral (18.46° and 20.32°), $Al(OH)_3$ (gibbsite: 21.5°, 29.43°, and 40.51°), SiO_2 (quartz: 26.79°, 54.04°, and 59.80°), Fe_2O_3

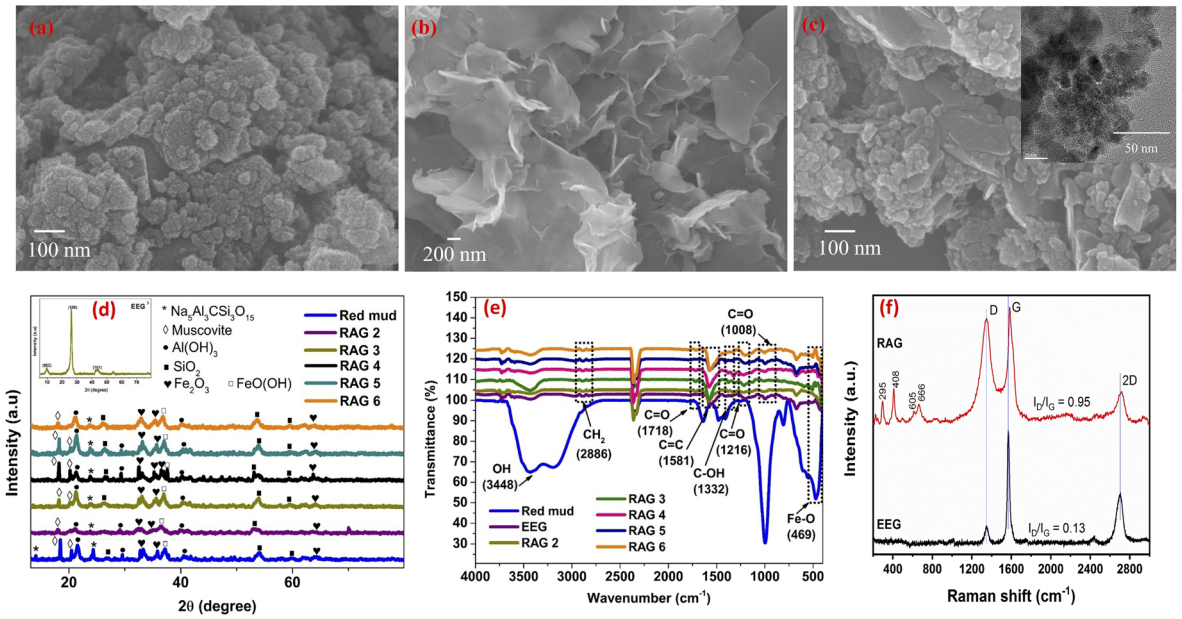

Fig. 2 SEM images of (a) red mud, (b) EEG, and (c) RAG, (d) XRD patterns and (e) FT-IR spectra of red mud and RAGs, and (f) Raman spectra of the EEG and RAG composite (inset in (d) is the XRD pattern of graphene flakes).

(hematite: 33.06°, 35.81°, and 64.22°), and FeO(OH) (geothite: 37.06°) in both RM and RAG samples, but the peak intensity also changed with electrochemical time. The sample of RAG3 appeared one more peaks of hematite at $2\theta = 36.6°$, proving the higher content of hematite which may be more beneficial for catalytic reaction.

In the FT-IR spectra as depicted in Fig. 2e, the peak at around 3448 cm^{-1} corresponds to the adsorption spectra of OH, whereas asymmetric and symmetric CH_2 stretching of graphene flakes can be seen at about 2886 cm^{-1}. The peak at 1581 cm^{-1} is considered to be the existence of C=C vibration and the peak at 1332 cm^{-1} is the presence of the C–OH bond of the carboxylic group. Besides, two peaks at around 1216 cm^{-1} and 1008 cm^{-1} are attributed to the vibrations of the C=O bond of the carboxylic group. When red mud was combined with graphene flakes, a new intense band C=O can be found at 1718 cm^{-1} belonging to RAGs nanocatalyst. Additionally, the peak at about 469 cm^{-1}, which corresponds to the Fe–O vibration of red mud[15,16] can be observed in FT-IR spectra of RAGs, demonstrating the synthesis of two raw materials by electrochemical process.

Raman spectroscopy in Fig. 2f was employed for further evaluation of exfoliated and activated graphite flakes, showing the characteristic D band at 1340 cm^{-1}, G band at 1570 cm^{-1}, and 2D band at 2685 cm^{-1} of graphene nanosheets.[17,18] In the case of the RAG composite, the Raman spectrum contains all D, G, and 2D peaks of graphene, and appears several peaks under the Raman shift of 1000 cm^{-1}, which could originate from vibrational mode assignments of metal oxides. In particular, the peaks at 295, 408, 605, and 666 cm^{-1} mostly correspond to the main component of hematite in red mud.[19,20] Moreover, the defects/disorders of the graphitic structure were evaluated through the intensity of the D band to G band (I_D/I_G). It is observed that the I_D/I_G of RAG 3 composite (0.95) is higher than that of EEG (0.13) due to the presence of various metal oxides that could damage the graphene surface or turn sp^2 hybridized-carbon atoms to sp^3 ones.[17] The shifting and broadening of G and 2D bands in RAG 3 composite as compared to that of EEG indicate the co-existence of graphene nanosheets and metal oxide species in RAG 3 composite,[20] which infers the successful production of graphene sheets by using red mud slurry as activating agent.

The N_2 adsorption–desorption isotherms and pore distribution of raw materials and RAG 3 are illustrated in Fig. S1 (see detail in SI). It can be seen that all isotherms belonged to type II according to the IUPAC classification, proving the interaction force between adsorbent and adsorbate is stronger than that of adsorbate and adsorbent. The pore is distributed mostly in the mesoporous range with size of 2–50 nm. Additionally, the BET surface area of RAG 3 composite and EEG are listed in Table S1 in SI, showing a remarkably higher value of RAG 3 composite as compared to that of EEG. This could be explained by the appearance of red mud components in the obtained composite after the electrochemical exfoliation process. Specifically, red mud is itself a porous material and can act as an appropriate agent for preventing the agglomeration of electrochemically exfoliated graphite flakes/graphene flakes, which significantly increases the specific surface area and enriches the pore structure of RAG 3 composite.[21] With higher surface area and other enhanced properties, it could be expected that RAG 3 composite will yield higher catalytic performance than distinct red mud and graphite components.

To better understand the surface chemical environment of RAG 3 composite, XPS measurement was conducted and results are exhibited in Fig. 3. As can be seen from Fig. 3a, the XPS spectrum reveals the presence of Al, Si, C, Ti, O, and Fe elements on the surface of RAG 3. The qualitative and quantitative chemical position of the RAG 3 composite is consistent with published literature, containing a mixture of hematite, quartz, gibbsite, and anatase.[22,23] Al 2p peak was observed at 74.5 eV, which might be assigned to gibbsite.[24] The peak at 102.4 eV could be attributed to the binding energy of Si 2p, revealing the formation of aluminosilicates or SiO_2.[25] Moreover, the characteristics of graphitic materials are evidenced by the presence of C=C (C sp^2, 284.4 eV) and C–C (C sp^3, 285.5 eV)[26] in Fig. 3b. Additionally, the oxygen defects were characterized by a C=O peak at 286.3 eV, corresponding to carbon atoms connected with oxygenated groups. Generally, the fitting results of the O 1s region showed three peaks Fig. 3c, indicating the presence of three kinds of oxygen species.[27] The first peak located at 530.1 eV is assigned to O–Fe from Me–O– lattice and the second peak observed at 531.8 eV corresponds to oxygen defect sites such as C=O groups which are mostly caused by the defect of graphite structure. The last peak at around 533.3 eV is attributed to C–O–C of epoxide group in graphene lattice.[28,29] Furthermore, the deconvolution of the Fe 2p line (Fig. 3d) shows a doublet and centers at binding energies of 711.2 eV (Fe^{2+} $2p_{3/2}$), 713.4 eV (Fe^{3+}), and 725.4 eV (Fe^{3+} $2p_{1/2}$). This result indicates that both Fe(III) and Fe(II) would exist concurrently[30,31] or Fe_3O_4 is the main iron phase on the surface of RAG 3 composite.[32,33] Beside, the energy separation between Fe $2p_{3/2}$ and Fe $2p_{1/2}$ was about 14.2 eV demonstrating the existence of Fe^{3+}. The small satellite peak at about 719.2 eV is ascribed to the presence of goethite and Fe(III) in γ-Fe_2O_3.[34] The detailed XPS analysis of Ti 2p is shown in Fig. 3e, where the deconvolution results depicts the Ti $2p_{3/2}$ and $2p_{1/2}$ signals at 462.0 eV and 466.7 eV, respectively. Besides, the separation ($\Delta = 2p_{1/2} - 2p_{3/2}$) was found to be 5.7 eV, which could be attributed to the Ti^{4+} oxidation state in TiO_2.[30]

The proposed mechanism formation of RAG 3 is described in 4 following steps. In the first step, water, by applying a bias voltage, is reduced at the cathode, creating hydroxyl radicals ($OH^{\bullet}$) alongside OH^- ions coming from the red mud slurry. Then, $OH^{\bullet}$ initially attacks the edge sites and grain boundaries of the graphite structure. In the second step, the depolarization and expansion of graphite layers might be attributed to the oxidation at the surface, for instance, at the edge sites and grain boundaries. This phenomenon could lead to intercalating sulfate ions (SO_4^{2-}) due to the expansion of the interlayer. During this stage, H_2O molecules and metal oxides might be co-intercalated in company with SO_4^{2-} ions. In the third step, various gases (*e.g.*, SO_2 and O_2) can be produced from the reduction of SO_4^{2-} ions, and self-oxidation of water, which is evidently by gaseous bubbles at anode electrode during the electrochemical method. The release of gaseous species could

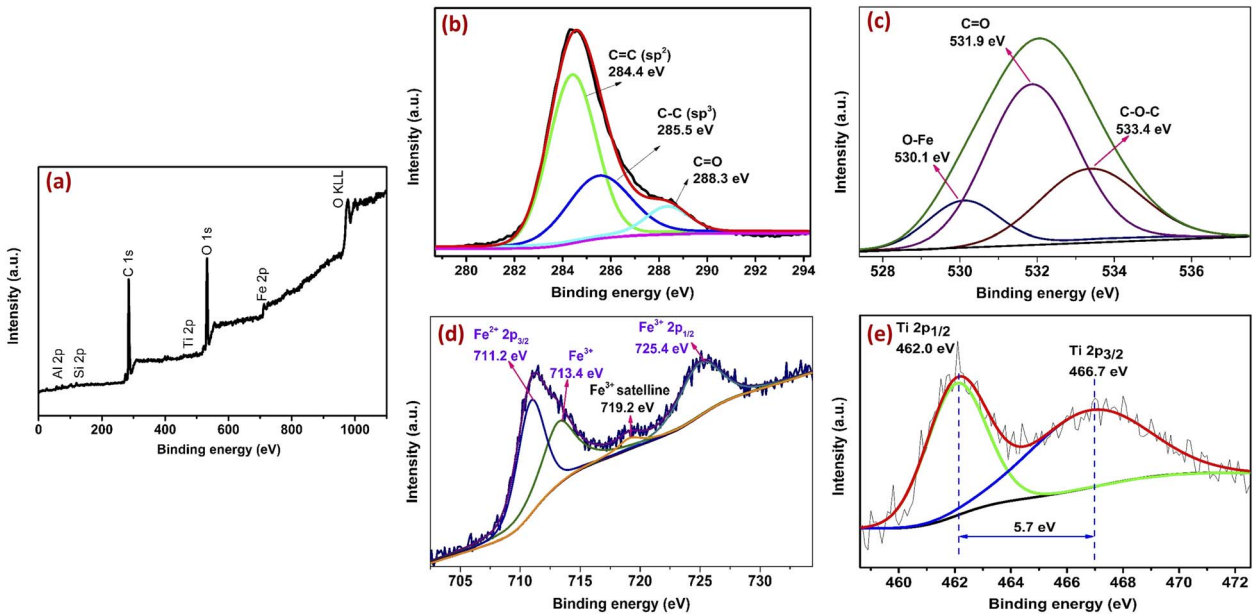

Fig. 3 (a) XPS survey and high resolution of (b) C 1s, (c) O 1s, (d) Fe 2p, and (e) Ti 2p in RAG 3 composite.

greatly extend graphite layers, which are able to break van der Waals bonding in graphite structure to form exfoliated graphite/graphene flakes. In the final step, during the electrochemical exfoliation and activation process, the surface of exfoliated graphite/graphene would be oxidized to create functionalized groups, which are directly associated with oxygen-containing groups (*e.g.* hydroxyl groups) on its surfaces.[35,36] Consequently, metal oxides (*e.g.*, TiO_2, Al_2O_3, SiO_2, and Fe_2O_3) would be anchored on the surface of the exfoliated graphite/graphene flakes through oxygen-bridge (*e.g.* C–O–Ti/Al/Fe/Si). Combined with graphene material, the composite formed by these oxides can be a catalyst for the decomposition reactions of pollutants in water.

3.2. Degradation of SMX by RAGs

3.2.1. Impact factors on SMX degradation efficiency. The effect of nanocatalysts, pH, sonication time, catalyst dosage, and temperature on the degradation of SMX with the support of ultrasound is exhibited in Fig. 4. It is obvious that the highest degradation capacity (lowest concentration ratio C_t/C_0) of SMX (Fig. 4a) can be observed by using RAG 3 (with $C_t/C_0 = 0.2480$ after 180 min). Meanwhile, the SMX degradation by RAG 2, RAG 4, RAG 5, and RAG 6 was only slightly improved in comparison with red mud due to low graphene flakes content (RAG 2). This leads to a lower adsorption capacity of SMX onto the surface of these nanocomposites, which then causes a lower degradation efficiency. Although graphene flakes exhibited no catalytic ability,[37] the removal efficiency of SMX using GO was dramatically higher than the figure of RAG 3 because the removal ability of SMX by graphene flakes is attributed to its high adsorption capacity. Therefore, RAG 3 was used as a catalyst for the next experimental investigations. In comparison with EEG, the C_t/C_0 ratio of RAG 3 was higher, however, EEG only exhibited the adsorption capability without catalytic activity.[38,39]

Fig. 4b indicates that higher degradation of SMX can be obtained at pH 3–5 with the highest efficiency of 74% and 77% after 180 min of sonication. Meanwhile, the degradation of SMX at pH 7–11 were declined dramatically with efficiency of <15%. It is obvious that SMX exists in protonated form (SMX^+) at pH ≤ 3.0, non-protonated form (SMX) at 3.0 < pH < 6.5, and deprotonated form at pH ≥ 6.5 (Fig. 4c).[40,41] Besides, at pH < 6.02, the surface of RAG 3 occupies a positive charge (RAG 3^+) while it is a negative charge at pH > 6.02 (RAG 3^-) and neutral (RAG 3) at pH = 6.02 (Fig. 4d). Thus, the effects that exist between the molecules of SMX and the surface of RAG 3 are summarized in Table 1. It is clear that at pH ≤ 3.0 and pH > 6.5, the repulsion effect presented between SMX^+ and RAG 3^+; SMX^- and RAG 3^-, whereas no effect can be found at 3.0 < pH < 6.5, thus the adsorption ability of SMX molecules onto the surface of catalyst was the best at 3.0 < pH < 6.5 reasoning the higher degradation efficiency of SMX.

Moreover, the catalyst dose also strongly affected the degradation efficiency of SMX (Fig. 4e). It can be seen that the removal efficiency of SMX increased with higher catalyst dosage. There was about 50.01% of SMX removed after 180 min by using 0.1 g L^{-1} of RAG 3, which then increased significantly to 91.17% with 0.5 g L^{-1} of catalyst. However, it decreased slightly to 86.78% with 0.6 g L^{-1} of RAG 3. Besides, Fig. 6f illustrates the impact of temperature on SMX degradation efficiency. As can be observed, higher efficiency can be obtained at higher temperatures (57.04%, 66.05%, and 77.20% at 30 °C, 40 °C, and 50 °C, respectively), demonstrating that the degradation reactions were endothermic. It can be confirmed by calculating the thermodynamic parameters.

3.2.2. Kinetics of the degradation process and reaction mechanism. The mineralization rate of the degradation reactions of SMX were calculated and summarized in Table 2. One can see that the pseudo-first-order kinetic model was more suitable to describe the kinetic of the SMX degradation process

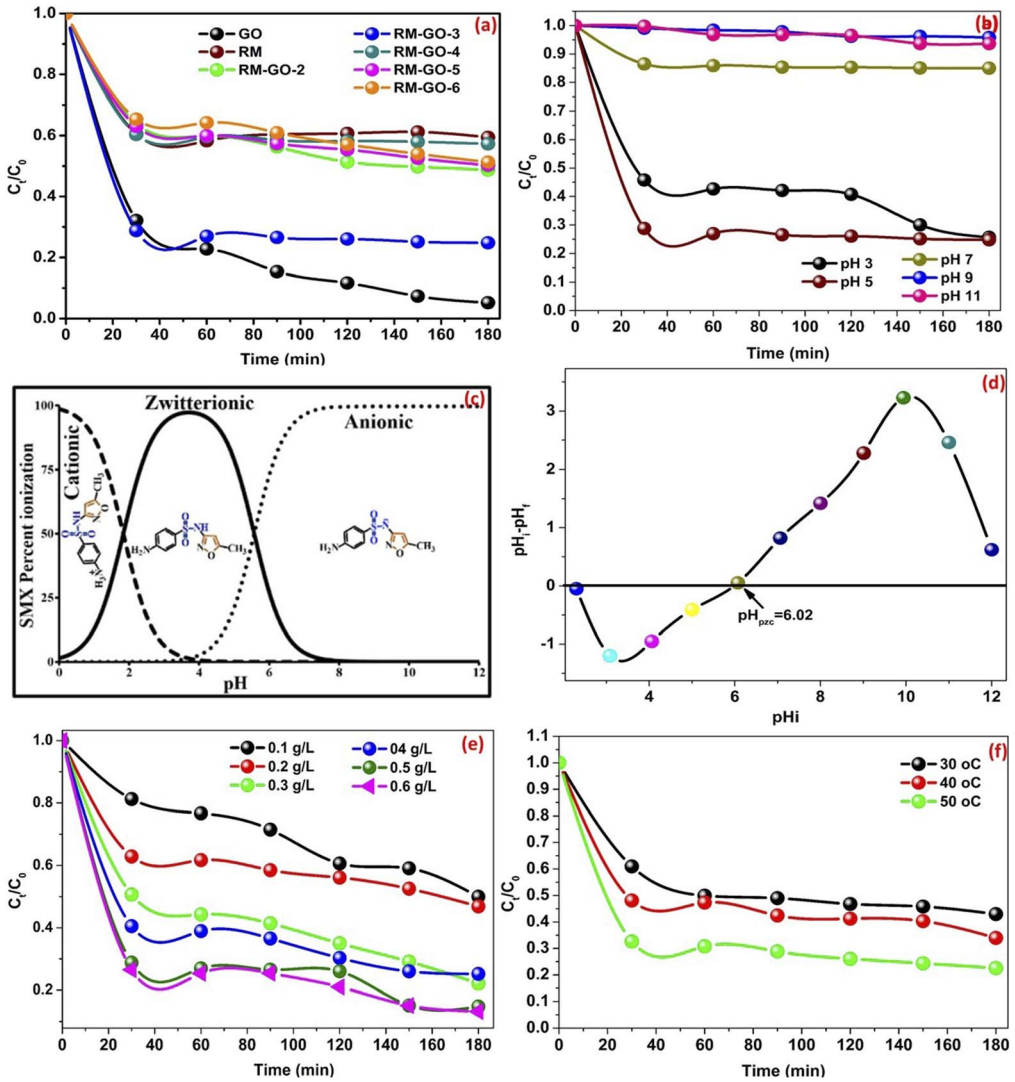

Fig. 4 Effect of sonocatalysts (a), sonication time (b), zwitterion form (c),[42] point of zero charge (d), catalyst mass (e), and temperature (f) on the degradation of SMX under ultrasound.

Table 1 Effect of pH on the existing forms of SMX and catalyst surface

pH	≤3.0	3–6.02	= 6.02	6.02–6.5	>6.5
SMX form	SMX^+	SMX	SMX	SMX	SMX^-
RAG 3 form	RAG 3^+	RAG 3^+	RAG 3	RAG 3^-	RAG 3^-
Effect	Repulsion	No effect	No effect	No effect	Repulsion

by RAG 3 at 40 °C ($R^2 = 0.9051$) and 50 °C ($R^2 = 0.9946$) than at 30 °C ($R^2 = 0.8371$). Additionally, the mineralization rate constant k increased with rising the reaction temperature from 30 °C to 50 °C (0.00196, 0.00214, and 0.00252 min^{-1}, respectively), proving the process is favorable at higher temperatures. In comparison with other researches,[43,44] the figures were relatively high (0.001 min^{-1} by UV/H_2O_2, and 0.0022 min^{-1} by UV/$Na_2S_2O_8$, 0.04089 ± 0.00754 min^{-1} with UV/O_3/Fe(II)). Although the values were lower than the number of UV/O_3/Fe(II), however, the utilization of red mud as raw material for synthesis of catalyst is one more dominant benefit.

Table 2 Pseudo-first-order kinetic models for degradation reactions of SMX

Temperature	Linear equation	R^2	k (min^{-1})
30 °C	$y = 0.5091 + 0.00196x$	0.8371	0.00196
40 °C	$y = 0.6439 + 0.00214x$	0.9051	0.00214
50 °C	$y = 1.0342 + 0.00252x$	0.9946	0.00252

To evaluate the kinetics of the degradation process, activation energy (E_a) is also a vital parameter. The E_a value was calculated based on the Arrhenius equation (Fig. S2) and summarized in Table 3. The activation energy of this reaction (E_a = 10.188 kJ mol^{-1}) was approximately the lowest one of diffusion of reactants (E_a = 10–30 kJ mol^{-1}),[45] indicating the reaction easily occurs. Besides, the enthalpy values ($\Delta H°$) of the reaction were positive at all investigated temperatures, exhibiting the endothermic process, while the entropy values ($\Delta S°$)

Table 3 Arrhenius parameters and thermodynamic parameters of the SMX degradation process

Arrhenius			
Equation	R^2	E_a (J mol^{-1})	A
$y = -2.204 - 1225.43x$	0.9642	10 188.23	9.06

Thermodynamic parameters				
Temperature (K)	ln A	$\Delta H°$ (J mol^{-1})	$\Delta S°$ (J mol^{-1})	$\Delta G°$ (J mol^{-1})
303	−2.204	7669.08	−271.68	89 989.54
313		7585.94	−271.95	92 707.74
323		7502.80	−272.22	95 428.61

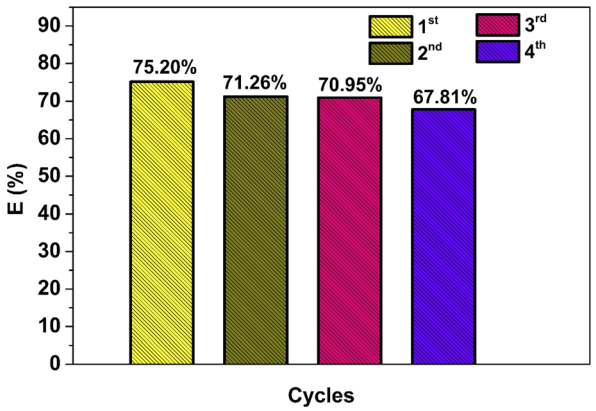

Fig. 6 Recycling experiments of degradation of SMX.

were negative, proving the process was becoming less disordered or the process required energy supply. Also, it will not occur spontaneously due to positive free Gibb energy values ($\Delta G°$).[46]

To confirm the formation of ˙OH and ˙OOH radicals which initated for the reactions of SMX during degradation process, the ethanol and ascorbic acid were used as scavenger of these radicals.[47] The result in Fig. 5a exhibited that without scavenger, the C_t/C_0 ratio was about 0.24, however, when ethanol or ascorbic acid was added, the degradation of SMX decreased moderately or C_t/C_0 increased signigicantly proving the important role of ˙OH and ˙OOH radicals in the degradation process of SMX with the support of ultrasound. Therefore, the result proves that the ˙OOH and ˙OH are the two vital active species in the degradation process of SMX.

Based on the scavenger experiment and analysis result, the proposed degradation mechanism of SMX using RAG 3 catalyst under ultrasound is illustrated in Fig. 5b. Under the effect of ultrasound, the bubbles are formed and grow the size following the compression–expansion cycles of ultrasound wave until the bubbles reach the maximum size and implode or collapse violently. The very high pressure and temperature are generated which excites H_2O and O_2 to form ˙OH and $^{\cdot}O_2^-$ radicals and initiates the degradation of SMX. A part of $^{\cdot}O_2^-$ radicals then reacts with H_2O to create ˙OH radicals whereas the remaining combines with H^+ for *in situ* introducing H_2O_2 (eqn (7)–(10)). After that, ˙OH and ˙OOH radicals are formed as the result of the reactions between H_2O_2 and Fe^{2+} or Fe^{3+} (eqn (11) and (12)).[39,48,49] The generated ˙OH and ˙OOH radicals initiated the degradation reactions of SMX (eqn (7) and (8)).

$$H_2O + \text{ultrasound} \rightarrow {}^{\cdot}H + {}^{\cdot}OH \quad (7)$$

$$O_2 + \text{ultrasound} \rightarrow {}^{\cdot}O_2^- \quad (8)$$

$${}^{\cdot}O_2^- + H_2O \rightarrow 2{}^{\cdot}OH \quad (9)$$

$${}^{\cdot}O_2^- + 2H^+ \rightarrow H_2O_2 \quad (10)$$

$$H_2O_2 + Fe^{2+} \rightarrow Fe^{3+} + {}^{\cdot}OH + OH^- \quad (11)$$

$$H_2O_2 + Fe^{3+} \rightarrow Fe^{2+} + {}^{\cdot}OOH + H^+ \quad (12)$$

$${}^{\cdot}OH + SMX \rightarrow \text{degraded products} \quad (13)$$

$${}^{\cdot}OOH + SMX \rightarrow \text{degraded products} \quad (14)$$

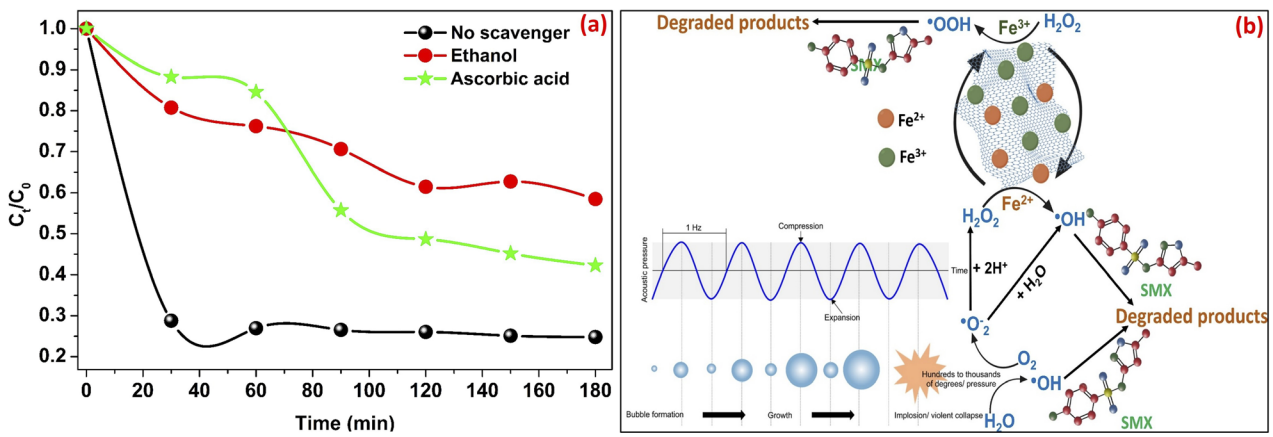

Fig. 5 Influence of various scavengers on the degradation of SMX (a), proposed mechanism for SMX degradation SMX using RAG 3 under ultrasound.

Table 4 The ability of RAG 3 for SMX degradation in comparison with other catalysts

No.	Catalysts	Synthesized conditions of material	Pollutants	Removal conditions of pollutant	Efficiency (%)	Ref.
1	Red mud/graphene oxide (RM-GO) composite	GO was synthesized by modified Hummer's method before being mixed with RM by ultrasound	Tetracycline (TC)	50 mg RM-7GO, 10 mg L^{-1} TC, visible light (λ > 420 nm), 300 W xenon lamp, 80 min 25 °C	79.8	50
2	RM-H/rGO composite	RM was treated by acid and calciunation to reduce the impurities in RM, making α-Fe_2O_3 active for H_2O_2 decomposing	Rhodamine B (RhB)	RM-H/rGO composite photo-Fenton catalyst, wide pH range, H_2O_2, 20 min	99.8	51
3	RAG 3	RAG 3 was synthesized by electrochemical method using red mud mixture as electrolyte and graphite rods as electrodes	Sulfamethoxazole (SMX)	0.5 g L^{-1} of RAG 3 catalyst under ultrasound, pH 5, 10 mg L^{-1} of SMX, 180 min	91.17	This research

3.2.3. Cycling behavior of RAG 3. The good stability and reusability of catalyst material is very vital for actual application. To test these by degrading SMX repeatedly for four times under same conditions including initial concentration of SMX (13 mg L^{-1}), volume of SMX solution (100 mL), catalyst mass (0.03 g), and ultrasound time (180 min). The result was illustrated in Fig. 6. Although the degradation efficiency of SMX by ultrasound-supported RAG 3 decreased slightly, which may cause by the mass loss of RAG 3 and the adsorption of SMX on the RAG 3's surface during process, the RAG 3 efficiency still remained high performance after four continuos cycles. The degradation efficiency of SMX by RAG 3 declined slightly from 75.20% ($C_t/C_0 = 0.25$) to 67.81% ($C_t/C_0 = 0.32$) demostrating the high stability and good recycle of RAG 3.

3.2.4. The comparative studies for the degradation of SMX with other materials. The ability of RAG 3 for SMX degradation was also evaluated by comparing it with other catalysts, as exhibited in Table 4. It is clear that the synthesis methods for other materials are relatively complex, requiring multiple steps and additional chemicals. In contrast, the degradation of SMX using ultrasound in the presence of RAG 3 is effective and comparable to that achieved with other materials. Moreover, the optimal pH for this process was improved to pH 5, demonstrating that RAG 3 is a more effective catalyst than the others.

4. Conclusions

This paper demonstrates a facile simultaneous electrochemical activation and exfoliation of a graphite rod in red mud slurry to anchor metal oxides on the graphene sheets. The obtained material was well characterized by SEM, TEM, XRD, Raman, FT-IR, BET, and XPS measurements. Moreover, the RAG product has very potential as a low-cost and effective catalyst for removing SMX antibiotic pollutants in water by sonodegradation with the highest removal efficiency of 91.2% at an SMX concentration of 10 mg L^{-1} and pH solution of 5.2. Besides, the SMX degradation reactions were endothermic with the highest rate constant of 0.00252 min^{-1}, low activation energy of 10.18 kJ mol^{-1}, unspontaneous reaction, and required energy supply. Regarding to high alkaline condition of red mud in their composition as an activating reagent, the present work provides a novel and efficient route for reducing the solid waste residue of bauxite production and a feasible, inexpensive, and simple production of highly effective sonocatalyst for the removal of organic compounds in wastewater.

Author contributions

Nguyen Thi Mai: conceptualization, investigation, writing – original draft, Le Thi Thanh Hoa, Nguyen Nhat Huy: data curation, methodology, formal analysis; Dang Van Thanh and Nguyen Manh Khai: conceptualization, resource, editing, Nguyen Thi Mai, Hoang Minh Trang, Tran Van Son: resource, methodology, investigation, Duc Dung Nguyen: formal analysis, writing – review, Pham Thi Thuy, Nguyen Thi An Hang, Tran Thi Minh Hang: conceptualization, investigation, data curation, Pham Thi Thuy, Nguyen Thi An Hang: data curation,

methodology, formal analysis, Nguyen Thi Mai: formal analysis and validation, Nguyen Nhat Huy: software, visualization, formal analysis, Dang Van Thanh and Nguyen Manh Khai: conceptualization, resource, writing and editing.

Conflicts of interest

There are no conflicts to declare.

Data availability

The supporting data has been submitted along with the manuscript and will be available as SI when the article online. See DOI: **https://doi.org/10.1039/d5ra04400f**.

Acknowledgements

This research is funded by Vietnam National Foundation for Science and Technology Development (NAFOSTED) under grant number 105.08-2021.32.

References

1 J. Wang and S. Kaskel, KOH activation of carbon-based materials for energy storage, *J. Mater. Chem.*, 2012, **22**, 23710–23725.
2 B. Bai, J. Chen, F. Bai, Q. Nie and X. Jia, Corrosion effect of acid/alkali on cementitious red mud-fly ash materials containing heavy metal residues, *Environ. Technol. Innovat.*, 2024, **33**, 103485.
3 C. Chen, D. Yu, G. Zhao, B. Du, W. Tang, L. Sun, Y. Sun, F. Besenbacher and M. Yu, Three-dimensional scaffolding framework of porous carbon nanosheets derived from plant wastes for high-performance supercapacitors, *Nano Energy*, 2016, **27**, 377–389.
4 Y. Li, M. van Zijll, S. Chiang and N. Pan, KOH modified graphene nanosheets for supercapacitor electrodes, *J. Power Sources*, 2011, **196**, 6003–6006.
5 L.-Y. Meng and S.-J. Park, Effect of heat treatment on CO2 adsorption of KOH-activated graphite nanofibers, *J. Colloid Interface Sci.*, 2010, **352**, 498–503.
6 T. R. Kemnic and M. Coleman, *Trimethoprim Sulfamethoxazole*, StatPearls Publishing, Treasure Island, FL, 2023.
7 NcfB Information, *Sulfamethoxazole-Trimethoprim, LiverTox: Clinical and Research Information on DrugInduced Liver Injury*, 2017, pp. , pp. 1–6.
8 E. Scholar, *Sulfamethoxazole, xPharm: The Comprehensive Pharmacology Reference*, 2007.
9 Y. Lauzurique, S. Miralles-Cuevas, M. Godoy, P. Sepúlveda, S. Bollo, A. Cabrera-Reina, C. Huiliñir, S. Malato, I. Oller and R. Salazar-González, Elimination of sulfamethoxazole by anodic oxidation using mixed metal oxide anodes, *J. Water Proc. Eng.*, 2023, **54**, 103922.
10 S. Liu, S. U. Hassan, H. Ding, S. Li, F. Jin, Z. Miao, X. Wang, H. Li and C. Zhao, Removal of sulfamethoxazole in water by electro-enhanced Co^{2+}/peroxydisulfate system with activated carbon fiber-cathode, *Chemosphere*, 2020, **245**, 125644.
11 L. A. Rodríguez-Blanco, R. Ocampo-Pérez, C. F. Gómez-Durán, J. P. Mojica-Sánchez and R. S. Razo-Hernández, Removal of sulfamethoxazole, sulfadiazine, and sulfamethazine by UV radiation and $HO^{\bullet}$ and $SO_4^{\bullet-}$ radicals using a response surface model and DFT calculations, *Environ. Sci. Pollut. Res.*, 2020, **27**, 41609–41622.
12 P. Motwani, R. K. Vyas, M. Maheshwari and S. Vyas, Removal of sulfamethoxazole from wastewater by adsorption and photolysis, *Nat. Environ. Pollut. Technol.*, 2011, **10**, 51–58.
13 G. Vinodha, P. Shima and L. Cindrella, Mesoporous magnetite nanoparticle-decorated graphene oxide nanosheets for efficient electrochemical detection of hydrazine, *J. Mater. Sci.*, 2019, **54**, 4073–4088.
14 N. Hidayah, W.-W. Liu, C.-W. Lai, N. Noriman, C.-S. Khe, U. Hashim and H. C. Lee, Comparison on graphite, graphene oxide and reduced graphene oxide: Synthesis and characterization, *AIP Conf. Proc.*, 2017, **1892**, 150002.
15 E. Mahmoudi, L. Y. Ng, W. L. Ang, Y. T. Chung, R. Rohani and A. W. Mohammad, Enhancing morphology and separation performance of polyamide 6, 6 membranes by minimal incorporation of silver decorated graphene oxide nanoparticles, *Sci. Rep.*, 2019, **9**, 1216.
16 R. A. Rochman, S. Wahyuningsih, A. H. Ramelan and Q. A. Hanif, Preparation of nitrogen and sulphur Co-doped reduced graphene oxide (rGO-NS) using N and S heteroatom of thiourea, *IOP Conference Series: Materials Science and Engineering*, IOP Publishing, 2019, p. 012119.
17 A. C. Ferrari, J. Meyer, V. Scardaci, C. Casiraghi, M. Lazzeri, F. Mauri, S. Piscanec, D. Jiang, K. Novoselov and S. Roth, Raman spectrum of graphene and graphene layers, *Phys. Rev. Lett.*, 2006, **97**, 187401.
18 S. Shivaraman, M. V. S. Chandrashekhar, J. J. Boeckl and M. G. Spencer, Thickness Estimation of Epitaxial Graphene on SiC Using Attenuation of Substrate Raman Intensity, *J. Electron. Mater.*, 2009, **38**, 725–730.
19 M. Hanesch, Raman spectroscopy of iron oxides and (oxy) hydroxides at low laser power and possible applications in environmental magnetic studies, *Geophys. J. Int.*, 2009, **177**, 941–948.
20 G. K. Pradhan, D. K. Padhi and K. Parida, Fabrication of α-Fe2O3 nanorod/RGO composite: a novel hybrid photocatalyst for phenol degradation, *ACS Appl. Mater. Interfaces*, 2013, **5**, 9101–9110.
21 O. Kazak, Y. R. Eker, I. Akin, H. Bingol and A. Tor, Green preparation of a novel red mud@carbon composite and its application for adsorption of 2,4-dichlorophenoxyacetic acid from aqueous solution, *Environ. Sci. Pollut. Res.*, 2017, **24**, 23057–23068.
22 A. Milenković, I. Smičiklas, N. Bundaleski, O. M. Teodoro, Đ. Veljović and N. Vukelić, The role of different minerals from red mud assemblage in Co (II) sorption mechanism, *Colloids Surf., A*, 2016, **508**, 8–20.
23 S. Smiljanić, I. Smičiklas, A. Perić-Grujić, B. Lončar and M. Mitrić, Rinsed and thermally treated red mud sorbents for aqueous Ni2+ ions, *Chem. Eng. J.*, 2010, **162**, 75–83.

24 J. T. Kloprogge, L. V. Duong, B. J. Wood and R. L. Frost, XPS study of the major minerals in bauxite: gibbsite, bayerite and (pseudo-) boehmite, *J. Colloid Interface Sci.*, 2006, **296**, 572–576.

25 C. Wagner, A. Naumkin, A. Kraut-Vass, J. Allison, C. Powell and J. Rumble Jr, *NIST Standard Reference Database 20*, Version 3.4 (Web version), National Institute of Standards and Technology, Gaithersburg, MD, 2003, p. 20899.

26 D. Van Thanh, L.-J. Li, C.-W. Chu, P.-J. Yen and K.-H. Wei, Plasma-assisted electrochemical exfoliation of graphite for rapid production of graphene sheets, *RSC Adv.*, 2014, **4**, 6946–6949.

27 N. Kruse and S. Chenakin, XPS characterization of Au/TiO2 catalysts: Binding energy assessment and irradiation effects, *Appl. Catal., A*, 2011, **391**, 367–376.

28 B. Xu, F. Qi, J. Zhang, H. Li, D. Sun, D. Robert and Z. Chen, Cobalt modified red mud catalytic ozonation for the degradation of bezafibrate in water: Catalyst surface properties characterization and reaction mechanism, *Chem. Eng. J.*, 2016, **284**, 942–952.

29 L. Li, P. Ma, S. Hussain, L. Jia, D. Lin, X. Yin, Y. Lin, Z. Cheng and L. Wang, FeS2/carbon hybrids on carbon cloth: a highly efficient and stable counter electrode for dye-sensitized solar cells, *Sustain. Energy Fuels*, 2019, **3**, 1749–1756.

30 M. C. Biesinger, L. W. M. Lau, A. R. Gerson and R. S. C. Smart, Resolving surface chemical states in XPS analysis of first row transition metals, oxides and hydroxides: Sc, Ti, V, Cu and Zn, *Appl. Surf. Sci.*, 2010, **257**, 887–898.

31 G. Li, X. Xu, R. Han and J. Ma, Synthesis and superior electrochemical properties of shaggy hollow Zn-doped Fe2O3 nanospheres for high-performance lithium-ion batteries, *CrystEngComm*, 2016, **18**, 2949–2955.

32 W. Kim, K. Kawaguchi, N. Koshizaki, M. Sohma and T. Matsumoto, Fabrication and magnetoresistance of tunnel junctions using half-metallic Fe3O4, *J. Appl. Phys.*, 2003, **93**, 8032–8034.

33 N. McIntyre and D. Zetaruk, X-ray photoelectron spectroscopic studies of iron oxides, *Anal. Chem.*, 1977, **49**, 1521–1529.

34 H. Wu, G. Gao, X. Zhou, Y. Zhang and S. Guo, Control on the formation of Fe3O4 nanoparticles on chemically reduced graphene oxide surfaces, *CrystEngComm*, 2012, **14**, 499–504.

35 Z.-S. Wu, W. Ren, L. Wen, L. Gao, J. Zhao, Z. Chen, G. Zhou, F. Li and H.-M. Cheng, Graphene anchored with Co3O4 nanoparticles as anode of lithium ion batteries with enhanced reversible capacity and cyclic performance, *ACS Nano*, 2010, **4**, 3187–3194.

36 G. Zhou, D.-W. Wang, L.-C. Yin, N. Li, F. Li and H.-M. Cheng, Oxygen bridges between NiO nanosheets and graphene for improvement of lithium storage, *ACS Nano*, 2012, **6**, 3214–3223.

37 H. Su, Q. Zhao, Y. Wang, Q. Zhao, C. Jang, Y. Niu, W. Lou and Y. Qi, SnO nanoparticles on graphene oxide as an effective catalyst for synthesis of lubricating ester oils, *Catal. Commun.*, 2022, **162**, 106370.

38 X. Jiao, Z. Sun and Z. Li, Improved electrochemical exfoliation multi-folded graphene for boosting the performance of Zn-ion supercapacitor, *Mater. Today Commun.*, 2024, **41**, 110996.

39 T. M. Nguyen, V. T. Dang, N. H. Nguyen, T. M. H. Tran, H. H. Ngo and M. K. Nguyen, Red mud supported on rice husk biochar as sono-photo-Fenton catalysts for degradation of ciprofloxacin in water, *Sep. Purif. Technol.*, 2024, 129039.

40 L. Hou, H. Zhang, L. Wang, L. Chen, Y. Xiong and X. Xue, Removal of sulfamethoxazole from aqueous solution by sono-ozonation in the presence of a magnetic catalyst, *Sep. Purif. Technol.*, 2013, **117**, 46–52.

41 J. C. Serna-Carrizales, A. I. Zárate-Guzmán, A. Aguilar-Aguilar, A. Forgionny, E. Bailón-García, E. Flórez, C. F. Gómez-Durán and R. Ocampo-Pérez, Optimization of binary adsorption of metronidazole and sulfamethoxazole in aqueous solution supported with DFT calculations, *Processes*, 2023, **11**, 1009.

42 M. Bizi, Sulfamethoxazole removal from drinking water by activated carbon: kinetics and diffusion process, *Molecules*, 2020, **25**, 4656.

43 A.-M. Wang, C.-H. Wu, S.-R. Jhu, C.-D. Dong, C.-W. Chen, Y.-L. Lin, G.-Y. Su and Y.-T. Tsai, Photodegradation of sulfonamides in UV/ozone, UV/oxidant, and UV/ozone/oxidant systems: comparison in terms of mineralization efficiency and power consumption, *Desalination Water Treat.*, 2021, **220**, 255–264.

44 C.-H. Wu, C.-D. Dong, C.-W. Chen and Y.-L. Lin, Mineralization of sulfamethoxazole by ozone-based and Fenton/Fenton-like-based processes, *React. Kinet. Mech. Catal.*, 2022, **135**, 441–457.

45 A. L. Petrou and A. Terzidaki, A meta-analysis and review examining a possible role for oxidative stress and singlet oxygen in diverse diseases, *Biochem. J.*, 2017, **474**, 2713–2731.

46 M. Kamran, *Fuel cell, Renewable Energy Conversion Systems*, 2021, pp. 221–242.

47 N. T. Mai, D. Van Thanh, N. N. Huy, D. D. Bich, T. T. M. Hang, N. H. Hao and N. M. Khai, Red mud supported on rice husk biochar as sono-photo-Fenton catalysts for degradation of ciprofloxacin in water, *Sep. Purif. Technol.*, 2025, **354**, 129039.

48 E. Brillas, I. Sirés and M. A. Oturan, Electro-Fenton process and related electrochemical technologies based on Fenton's reaction chemistry, *Chem. Rev.*, 2009, **109**, 6570–6631.

49 R. Ovalle, *A history of the Fenton reactions (Fenton chemistry for beginners), Reactive Oxygen Species 1*, 2022.

50 H.-j. Ren, Y.-b. Tang, W.-l. Shi, F.-y. Chen and Y.-s. Xu, Red mud modified with graphene oxide for enhanced visible-light-driven photocatalytic performance towards the degradation of antibiotics, *New J. Chem.*, 2019, **43**, 19172–19179.

51 X. An, Z. Hou, Y. Yu, J. Wang, H. Lan, H. Liu and J. Qu, Red mud supported on reduced graphene oxide as photo-Fenton catalysts for organic contaminant degradation, *Colloids Surf., A*, 2022, **640**, 128461.